

# ECAMP: Entity-centered Context-aware Medical Vision Language Pre-training

Rongsheng Wang<sup>1,3,5\*</sup> Qingsong Yao<sup>3,4\*</sup> Haoran Lai<sup>2,3,5</sup> Zhiyang He<sup>5</sup>  
Xiaodong Tao<sup>5</sup> Zihang Jiang<sup>2,3†</sup> S. Kevin Zhou<sup>2,3,4†</sup>

<sup>1</sup> School of Computer Science and Technology, University of Science and Technology of China

<sup>2</sup> School of Biomedical Engineering & Suzhou Institute for Advanced Research, University of Science and Technology of China

<sup>3</sup> Center for Medical Imaging, Robotics, Analytic Computing & Learning (MIRACLE).

Suzhou Institute for Advanced Research, University of Science and Technology of China

<sup>4</sup> Key Lab of Intelligent Information Processing of Chinese Academy of Sciences (CAS), Institute of Computing Technology

<sup>5</sup> Anhui IFLYTEK CO., Ltd.

{rongsheng\_wang, Haoranlai}@mail.ustc.edu.cn

{jzh0103, skevinzhou}@ustc.edu.cn

yaoqingsong19@mails.ucas.edu.cn

**Abstract.** Despite significant advancements in medical vision-language pre-training, existing methods have largely overlooked the inherent entity-specific context within radiology reports and the complex cross-modality contextual relationships between text and images. To close this gap, we propose a novel Entity-centered Context-aware Medical Vision-language Pre-training (ECAMP) framework, which is designed to enable a more entity-centered and context-sensitive interpretation of medical data. Utilizing the recent powerful large language model, we distill entity-centered context from medical reports, which enables ECAMP to gain more effective supervision from the text modality. By further pre-training our model with carefully designed entity-aware, context-enhanced masked language modeling and context-guided super-resolution tasks, ECAMP significantly refines the interplay between text and image modalities, leading to an enhanced ability to extract entity-centered contextual features. Besides, our proposed multi-scale context fusion design also improves the semantic integration of both coarse and fine-level image representations, prompting better performance for multi-scale downstream applications. Combining these components leads to significant performance leaps over current state-of-the-art methods and establishes a new standard for cross-modality learning in medical imaging, whose effectiveness is demonstrated by our extensive experiments on various tasks including classification, segmentation, and detection across several public datasets. Code and models are available at <https://github.com/ToniChopp/ECAMP>.

**Keywords:** medical vision-language pre-training · masked modeling

## 1 Introduction

By virtue of its exceptional accuracy and efficiency, deep learning (DL) is increasingly pivotal in medical image analysis [13, 14, 39, 46, 64]. However, precision is contingent upon large-scale and high-quality annotations, which require an extensive number of experienced medical professionals, rendering it a costly endeavor. Fortunately, the diagnosis and experiential knowledge [40] of radiologists are preserved in the form of paired reports and images, which provide valuable semantic context for training DL-based models. More notably, these supervised signals are relatively accessible at little to no additional costs.

Cutting-edge algorithms [1] in medical vision-language pre-training (Med-VLP) primarily leverage the information-rich medical report-image pairs to learn generic representations from two aspects: *contrastive-based* methods align the text and image features at both global [61] and local [17, 49] levels; while *reconstruction-based* methods generate the masked words [11] and image patches [15] using cross-modality information [63]. Nevertheless, these methods still exhibit limitations in harnessing the potential of supervision in the report context. First, the linguistic challenge [22] posed by complex biomedical context [29] impedes the effectiveness of pre-training [2]. Second, radiologists often include diagnoses for common diseases (e.g., pneumothorax) in their reports, even when these diseases are negative [10]. This results in a significant context imbalance issue [2]: the majority of disease diagnoses are negative<sup>1</sup>, introducing an adverse bias into the optimization of masked language modeling (MLM) [11].

In this paper, we introduce **Entity-Centered Context-Aware Medical vision-language Pre-training (ECAMP)**, a robust pre-training framework for radiology. As shown in Fig. 1, ECAMP consists of four simple-yet-effective components: 1) *entity-aware context distillation*, 2) *entity-centered context-enhanced MLM*, 3) *context-guided super-resolution*, and 4) *multi-scale context fusion*. Su-

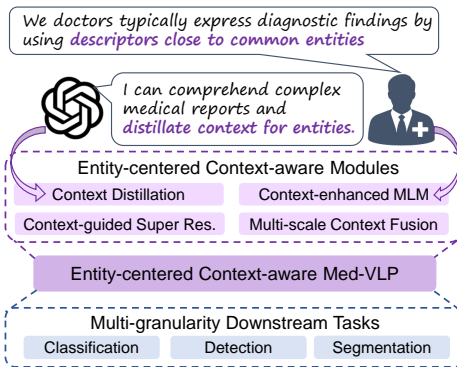


**Fig. 1:** Our ECAMP obtains medical knowledge from ChatGPT and experts respectively, centered on entities including diseases and symptoms, etc. *Context distillation* asks ChatGPT to distillate precise content for entities, while *Context-enhanced MLM* predicts the masked descriptors close to entities and addresses the imbalance difficulty caused by doctors’ habits. Further, ECAMP develops *Multi-scale Context Fusion* to learn global and local projections simultaneously for multi-granularity downstream tasks.

<sup>1</sup> Statistical results of the imbalanced diagnosis descriptors can be found in the supplementary materials.

terior to PRIOR [7] which substitutes complex biomedical sentences with prototypes, we propose *entity-aware context distillation* to distill context from Large Language Model in the form of text, leveraging its strong power in linguistic comprehensive and summarizing [36]. Specifically, we use ChatGPT [3] to summarize the complex reports into succinct expressions with entity diagnosis (like “There may be pneumonia.”), which facilitates more effective supervision of the complex reports in pre-training. Furthermore, based on our consultations with medical professionals [10], radiologists typically express diagnostic findings by using descriptors close to Medical Subject Headings (MeSH) [30] entities (e.g., pneumonia). Accordingly, we propose *entity-centered context-enhanced MLM*, employing a fixed masking strategy to optimize the pre-trained model to predict these key descriptors. To tackle the imbalance problem, we further add an effective re-balanced factor for the minority of the positive descriptors, which prevents the model from ignoring the critical positive diagnoses in reports.

Moreover, super-resolution exhibits promise as a self-supervised proxy task [63]. Given that critical pathology usually occupies small patches, we hypothesize that learning to reconstruct these subtle cues helps to better understand pathology and hence leads to better performance. Fortuitously, leveraging the concise distilled reports, we can retrain patch-level contrastive-based methods [17] to procure precise entity-specific attention maps. These maps facilitate our proposed *context-guided super-resolution* to learn the high-resolution characteristics of the target pathology with broader contextual information, thereby enabling a more holistic and accurate interpretation of medical images.

In addition, we find current cross-modal reconstruction-based methods typically employ either global average pooling (GAP) [63] or cross-attention [6] to integrate global and local vision representations to assist MLM. In contrast, we introduce *multi-scale context fusion* to aggregate global and local projection of pre-trained vision encoder simultaneously. Our motivation is to learn both global and local informative representations, which can be generalized to a wide range of multi-scale downstream tasks, including classification, segmentation, and detection.

We pre-train ECAMP on MIMIC-CXR [19] dataset consisting of image-report pairs. Extensive experiments are conducted on multi-scale downstream tasks (including classification, segmentation, and detection) across multiple public datasets, e.g., ChestX-ray14 [51], CheXpert [18], RSNA Pneumonia [43], COVIDx [50] and SIIM Pneumothorax [44] to demonstrate the superiority of ECAMP compared with a plethora of competitive state-of-the-art Med-VLP methods with a significant performance gap, whose readily accessible components prove valuable in fortifying the establishment of a foundational medical model.

## 2 Related Work

### 2.1 General Vision Language Pre-training

Vision-language pre-training (VLP) aims to improve the performance of multi-granularity downstream vision and language tasks by pre-training the model on large-scale image-text pairs. Tremendous success has been achieved in recent literature, which can be summarized into two groups: encoder-based [24, 26], or encoder-decoder based [9, 52] models. One of the most representative encoder-based methods is CLIP [41], which shows a great potential for learning mutual information between visual and linguistic data. Recently, more works (e.g. GLIP [25], SLIP [35], FLIP [28], OSCAR [27], and VinVL [58]) indicate that fine-grained context alignment facilitates the model to learn more representative representations. For the encoder-decoder methods, BLIP [23] leverages a decoder to reconstruct text by leveraging vision semantic context. In this paper, we focus on the challenging medical domain, where medical report is harder to comprehend and accuracy is more of paramount importance.

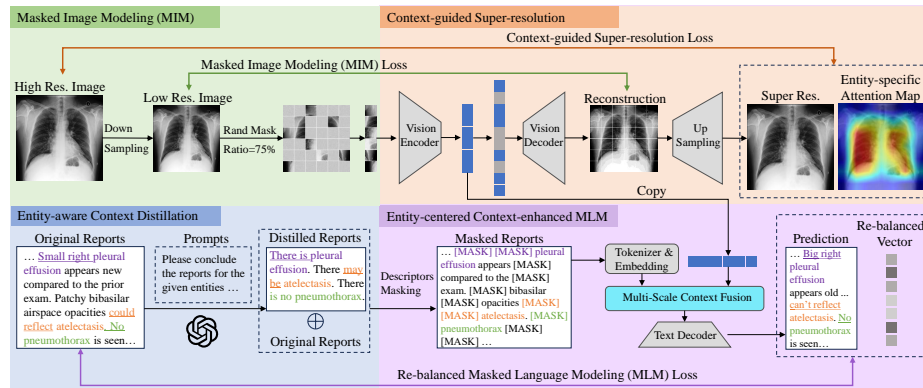


**Fig. 2:** The overall framework of our ECAMP. Initially, *entity-aware context distillation* succinctly encapsulates precise diagnosis for each entity. Then *entity-centered context-enhanced MLM* masks the two descriptive words (underlined) preceding the entity, employing a re-balanced vector to direct the model’s attention towards critical minority-positive expressions. To further enhance the learning of pathology vision contexts, *context-guided super-resolution* utilizes an entity-specific attention map. Finally, we introduce a novel *multi-scale context fusion* block (highlighted in cyan) to concurrently capture representative global and local features.

### 2.2 Medical Vision Language Pre-training

Recent Med-VLP methods can be categorized into two distinct types: report-supervised cross-modal alignment pre-training and reconstruction-based self-supervised pre-training. The groundbreaking works of the former type such as ConVIRT [61], REFERS [62], and CheXZero [47] pre-train the model by directly maximizing mutual information between the global representations. GLORIA [17], SAT [31], and MGCA [49] propose to align fine-grained features of

paired image patches and words. PRIOR [7] and BioVIL [2] attempt to comprehend intricate medical reports. MedKLIP [54] and KAD [60] extract the medical-related information using a triplet extraction module as additional supervised signals. Inspired by BERT [11] and MAE [15], the latter type learns representation by cross-modal context reconstruction task. M3AE [6] utilizes cross-attention for integrating multi-modal information to reconstruct masked tokens. While MRM [63] directly applies global average pooling for fusing visual features for masked text modeling. Further, MPMA [57] introduces a memory-augmented cross-modal fusion module to fully integrate visual information to assist report reconstruction.

Advanced efforts try to combine contrastive-based and reconstruction-based pre-training. CMITM [5] contrastively aligns global report and image representations after pre-training with MRM [63], while MedIM [56] boosts MGCA [49] with attention guided masked image modeling. Notwithstanding the enhancements, the aforementioned approaches are constrained by the intricacies of comprehending biomedical reports and the imbalance in diagnoses, which has spurred our pursuit of developing ECAMP. Med-Unic [48] and Med-MLLM [32] further improve the performance by leveraging more pre-training datasets.

### 2.3 Large Language Models (LLMs)

Compared to BERT [11], recent LLMs such as GPT-3 [3] have a much larger scale in terms of training data and model parameters. This scale affords them robust zero-shot generalization capabilities to comprehend previously unseen contexts. Further, instruction-tuning [37, 42] is proposed to effectively improve the performance of LLM in novel application scenarios, including news summarization [59] and code summarization [45]. Luckily, advanced LLMs such as ChatGPT [3] also exhibit robust capabilities in complex biomedical contexts. To the best of our knowledge, we are among the first few works to distill medical knowledge from medical reports using LLMs.

## 3 Method

In this section, we first introduce how ECAMP leverages *context distillation* to distill distinct context from LLM in Sec. 3.1. Then, we illustrate the basic masked image modeling (MIM) [15] and the proposed *entity-centered context-enhanced MLM* in Sec. 3.2. Next, Sec. 3.3 shows the process of *context-guided super-resolution*. Finally, we clarify the detailed approaches of *multi-scale context fusion* in Sec. 3.4 to integrate both global and local vision features for MLM.

### 3.1 Context Distillation

Given an image  $I^o \in \mathbb{R}^{H^o \times W^o}$  and its original paired report  $T_o$ , Our target is to extract concise diagnosis for diseases from  $T_o$ . Accordingly, we select the set of entities  $R = \{r^1, r^2, \dots, r^k\}$  from MeSH [30], representing the diseases of

interest in chest radiography. For each original report  $T_o$ , we identify entities  $\mathbf{r}_o$  mentioned in the report through string matching. Next, prompt  $p$  is designed to require LLM to comprehend the complex biomedical context and summarize the diagnosis for disease entities  $\mathbf{r}_o$ . Furthermore, to make the summarization of LLM stable, we leverage in-context learning [34] to construct an one-shot [53] sample  $p'$  in the final prompt<sup>2</sup>  $p = P(T_o, \mathbf{r}_o, p')$ . The distilled report  $T_d$  is finally computed as follows:

$$T_d = \text{LLM}(P(T_o, \mathbf{r}_o, p')). \quad (1)$$

### 3.2 Masked Image and Language Modeling

**Masked image modeling** We first down-sample the original image  $I^o$  into high-resolution  $I^h \in \mathbb{R}^{H^h \times W^h}$  and low-resolution  $I^l \in \mathbb{R}^{H^l \times W^l}$  input. The low-resolution image  $I^l$  is split into  $N_p$  patches with size  $P \times P$ . Following MAE [15], we mask a large ratio (75%) of the  $N_p^I$  low-resolution patches, resulting in the unmasked patches  $I_u = \{I_u^1, I_u^2, \dots, I_u^{N_u^I}\}$  and masked patches  $I_m = \{I_m^1, I_m^2, \dots, I_m^{N_m^I}\}$ . Then the patch embedding  $E_p$  is obtained by linearly projecting the flattened unmasked patches  $I_u$ . Vision transformer [12] (ViT) is chosen as the vision encoder  $E_I$ , which projects the patch embedding  $E_p$  along with its positional embedding  $E_{pos}$  as the vision feature  $f_v = E_I(I_u, E_{pos})$ . In the image decoding procedure,  $f_v$  is fed into an image decoder  $D_I$  after recovering to the original  $N_p$  size, resulting in reconstructed image  $\hat{I}^l = D_I(E_I(I_u))$ . We choose mean square error (MSE) loss to optimize the reconstructed image:

$$\mathcal{L}_{\text{MIM}}(\hat{I}^l, I_m) = \text{MSE}(D_I(E_I(I_u)), I_m). \quad (2)$$

**Entity-centered context-enhanced MLM** For the paired report  $T_o$ , we concatenate the distilled report  $T_d$  as the text input  $T = [T_o, T_d]$ . As shown in Fig. 1, we mark the first  $\beta$  words preceding the entity  $R$  as “descriptive words”  $T_a = \{t_a^1, t_a^2, \dots, t_a^{N_a^T}\}$ . Based on practical experience, the majority of descriptive words used by doctors are located within the first two words preceding the entity words, e.g., “There is mild pneumonia.”, we set  $\beta$  to 2. Instead of using random masking [6, 11, 63], ECAMP introduces a naive-yet-effective “descriptors masking” to mask the tokens of descriptive words, compelling the network to predict the diagnosis of the doctors for each entity. The remaining words are randomly masked with a ratio of 75% to get masked words  $T_m = \{t_m^1, t_m^2, \dots, t_m^{N_m^T}\}$  and unmasked words  $T_u$ , and the masked words are replaced with [MASK] for training. WordPiece [55] is chosen as tokenizer to convert  $T$  into text tokens. Text embeddings  $E_t$  are further computed by projecting the text tokens and adding the encoded position information.

A high text masking ratio challenges the model to reconstruct the reports by encoding the vision context thoroughly and accurately. Accordingly, a novel

<sup>2</sup> The selected entities of disease and detailed prompt can be found in the Appendix.B and Appendix.C, respectively.

*multi-scale context fusion* module (MSCF, see Sec. 3.4) is proposed to integrate the vision feature and text embedding  $f_f = \text{MSCF}(f_v, E_t)$ . The reconstructed text  $\hat{T}$  is generated by decoding the fused feature  $f_f$  using a BERT-based [11] text decoder  $\hat{T} = D_t(f_f)$ . The MLM loss for each masked word  $t \in [T_m, T_a]$  is defined as  $\mathcal{L}_{\text{MLM}}^t(\hat{t}, t) = -\log(P(\hat{t} = t))$ .

Moreover, we simply categorize  $T_a$  into two groups: negative descriptions  $T_{neg}$  and others  $T_{oth}$ , with  $N_{neg}^T$  and  $N_{oth}^T$  words, respectively. Please note that since the expressions of positive descriptors are diverse, we divide them into others  $T_{oth}$ . To focus on modeling the minority-positive disease descriptions instead of majority-negative words, we multiply the loss of  $T_{neg}$  by a small number  $\lambda_{neg}$ , and the loss of  $N_{oth}^T$  by  $\lambda_{oth}$ , where

$$\lambda_{neg} * N_{neg}^T + \lambda_{oth} * N_{oth}^T = N_a^T. \quad (3)$$

According to the statistical results in Appendix.A, the most negative descriptor “there is no” occurs approximately 20× more often than the most positive descriptor “there may be.”, we set  $\lambda_{neg} = 0.05$ . Please note that  $\lambda_{oth}$  is important to make sure that the model pays an enough attention to accurately reconstruct the critical “descriptive words”  $T_a$ . The final loss of entity-centered context-aware MLM is defined:

$$\begin{aligned} \mathcal{L}_{\text{MLM}} = & \sum_j^{N_m^T} \mathcal{L}_{\text{MLM}}^t(\hat{t}_m^j, t_m^j) + \sum_j^{N_{neg}^T} \lambda_{neg} \mathcal{L}_{\text{MLM}}^t(\hat{t}_{neg}^j, t_{neg}^j) \\ & + \sum_j^{N_{oth}^T} \lambda_{oth} \mathcal{L}_{\text{MLM}}^t(\hat{t}_{oth}^j, t_{oth}^j). \end{aligned} \quad (4)$$

### 3.3 Context-guided Super-resolution

Using the entity-centered distilled report  $T_d$ , we re-train the SOTA fine-grained representation contrastive learning method GloRIA [17] to generate entity-specific attention map  $A$  for image  $I^h$ . Then, an up-sampling module  $D_{\text{SR}}$  up-scales the reconstructed image  $\hat{I}^l$  to the high-resolution results  $\hat{I}^h$ , which consists of a bi-linear interpolation and two convolution layers with a residual connection. As the model should focus on generating disease-relevant visual textures, we use the attention map as the guidance for super-resolution (SR). The SR loss function is as follows:

$$\mathcal{L}_{\text{SR}}(\hat{I}^h, I^h) = \text{MSE}(D_{\text{SR}}(D_I(E_I(I_u))), I^h | A), \quad (5)$$

The overall loss function of ECAMP is:

$$\mathcal{L} = \mathcal{L}_{\text{MIM}} + \mathcal{L}_{\text{MLM}} + \mathcal{L}_{\text{SR}}. \quad (6)$$

### 3.4 Multi-scale Context Fusion

**Table 1:** Evaluating our method against other SOTA Med-VLP approaches on the fine-tuning classification task. † denotes we reproduce results using their officially released models. Methods with # leverage disease-level annotations. The best and second-best results are **bolded** and underlined.

Method	CXR14 (AUC)			CXP (AUC)			RSNA (AUC)			COVIDx (ACC)		
	1%	10%	100%	1%	10%	100%	1%	10%	100%	1%	10%	100%
Random init	60.0	65.2	72.8	70.4	81.1	85.8	71.9	82.2	88.5	64.2	75.4	87.7
ImageNet init	69.8	74.4	80.0	80.1	84.8	87.6	83.1	87.3	90.8	72.0	84.4	90.3
<i>CNN-based</i>												
GLoRIA [17]	70.7	78.6	84.1	86.6	87.8	88.1	86.1	88.0	88.6	73.3	86.8	90.5
†SAT [31]	67.4	79.3	83.7	86.3	88.0	88.2	86.7	87.5	89.0	75.0	88.5	94.3
PRIOR [7]	75.7	79.4	84.3	86.2	88.3	88.6	85.7	87.1	89.2	<u>79.5</u>	89.8	94.8
MedKLIP# [54]	77.2	78.9	83.2	87.1	88.4	88.6	87.3	88.0	89.3	78.3	88.8	95.3
KAD [60]	78.7	80.7	82.5	87.2	88.2	88.5	89.8	91.8	92.5	78.5	90.5	<u>95.8</u>
<i>ViT-based</i>												
MAE [15]	74.7	81.3	85.1	80.7	86.0	86.7	84.2	89.6	91.3	69.8	82.3	90.8
GLoRIA [17]	77.7	82.8	85.0	86.5	87.5	87.8	89.7	91.2	92.1	76.8	<u>91.8</u>	94.8
REFERS [62]	76.7	80.9	84.7	87.2	88.1	88.2	89.4	91.6	92.7	76.5	90.8	94.5
MGCA# [49]	78.2	82.7	85.0	87.0	88.4	88.5	90.7	92.6	<u>93.4</u>	75.2	91.5	94.3
MRM [63]	<u>79.4</u>	<u>84.0</u>	<u>85.9</u>	<u>88.5</u>	<u>88.5</u>	<u>88.7</u>	<u>91.3</u>	<u>92.7</u>	93.3	78.0	90.3	92.5
ECAMP (Ours)	<b>81.9</b>	<b>85.1</b>	<b>86.7</b>	<b>88.8</b>	<b>89.5</b>	<b>89.7</b>	<b>91.5</b>	<b>93.2</b>	<b>94.2</b>	<b>83.0</b>	<b>95.5</b>	<b>97.5</b>

Different from MRM [63] which directly adds the vision feature  $f_v$  to the text embedding  $E_t$ , we first apply a self-attention (SA) for an initial comprehension of text embedding  $f_t = \text{SA}(E_t)$ . In order to simultaneously attain representative global and local features for multi-scale downstream tasks, we leverage patch-wise vision features  $f_v$  as local vision features  $f_v^l$  and use global average pooling (GAP) to compute global vision feature ( $f_v^g = \text{GAP}(f_v^l)$ ). Next, we aggregate local vision context  $f_v^l$  with text feature  $f_t$  by cross-attention (CA) to generate local aggregated feature  $f_a^l = \text{CA}(f_v^l, f_t)$ , and project the  $f_v^g$  by a linear projector to obtain global feature  $f_a^g$ . Finally, we integrate text feature  $f_t$ , local aggregated feature  $f_a^l$ , and duplicate global feature  $f_a^g$  by addition.

**Fine-tuning stage:** ECAMP takes the full images as input without masking in this stage. Our multi-scale context fusion design enables the model to learn

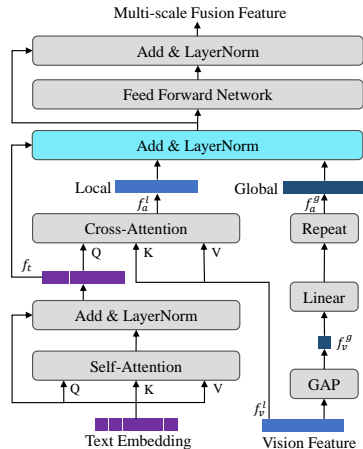


**Fig. 3:** The framework of *multi-scale context fusion*. The addition operation (highlighted in cyan) concurrently fuses the text feature, local aggregated vision feature, and global vision feature.

**Table 2:** Comparison with other state-of-the-art methods on the linear probe classification task. † means performances in CXR14 [51] and methods like MRM [63] are fine-tuned using their official released models. Methods with # leverage disease-level annotations, while Med-UniC [48] uses external additional pre-training data. The best and second-best results are **bolded** and underlined.

Method	†CXR14 (AUC)			CXP (AUC)			RSNA (AUC)			COVIDx (ACC)		
	1%	10%	100%	1%	10%	100%	1%	10%	100%	1%	10%	100%
Random init	52.1	54.6	55.3	56.1	62.6	65.7	58.9	69.4	74.1	50.5	60.3	70.0
ImageNet init	67.0	67.5	71.6	74.4	79.7	81.4	74.9	74.5	76.3	64.8	78.8	86.3
<i>CNN-based</i>												
SAT [31]	74.4	79.2	81.8	86.9	88.3	88.6	87.4	89.2	90.2	74.5	84.8	89.3
†PRIOR [7]	74.9	79.5	82.1	86.3	86.7	87.3	88.2	90.4	90.7	74.8	85.0	89.8
MedKLIP# [54]	78.5	80.9	83.2	86.2	86.5	87.7	88.1	90.8	92.0	74.5	85.3	90.3
†KAD [60]	78.1	79.8	81.6	86.4	86.9	87.8	87.9	90.0	91.3	75.0	84.3	90.5
Med-UniC [48]	-	-	-	88.2	89.2	<u>89.5</u>	89.1	90.4	90.8	76.5	89.0	92.8
<i>ViT-based</i>												
MAE [15]	75.1	79.7	82.9	82.4	84.6	85.2	86.5	89.7	90.2	79.0	88.5	92.5
GLoRIA [17]	77.0	81.9	83.8	84.6	85.8	86.2	87.2	88.1	88.9	73.3	87.7	92.1
MGCA# [49]	78.7	82.7	84.1	88.8	89.1	<b>89.7</b>	89.1	89.9	90.8	74.8	84.8	92.3
†MRM [63]	<u>78.8</u>	<u>82.7</u>	<u>84.6</u>	88.1	88.1	88.3	90.9	92.5	92.5	76.8	89.0	92.8
MedIM [56]	-	-	-	88.9	89.3	<b>89.7</b>	-	-	-	77.2	<u>90.3</u>	93.6
ECAMP (Ours)	<b>81.0</b>	<b>83.8</b>	<b>85.1</b>	<b>89.3</b>	<b>89.4</b>	<b>89.7</b>	<b>91.4</b>	<b>92.9</b>	<b>93.5</b>	<b>86.3</b>	<b>95.0</b>	<b>96.0</b>

compact global representation as well as informative fine-level local representation. For the high-level downstream task like classification, we fine-tune the global vision feature  $f_v^g$ . For the low-level vision tasks including segmentation and detection, we fine-tune the local vision features  $f_v^l$ . Thanks to the expressive representation, we are able to achieve impressive performance across different level vision tasks.

## 4 Experiment

### 4.1 Pre-training Dataset

MIMIC-CXR 2.0.0 [19, 20] contains 377,110 chest radiographs and 227,835 corresponding reports. Each report may be associated with one or more images captured from frontal, back, and lateral views. We extract detailed descriptions of medical diseases by focusing on the impression and finding sections in the free-text reports.

### 4.2 Downstream Tasks Datasets

**ChestX-ray14 (CXR14)** [51] comprises 112,120 frontal-view chest radiographs, and introduces a multi-label classification task involving *14 common chest pathologies*. The dataset is officially split into training, validation, and testing subsets with a ratio of 70%/10%/20%.

**CheXpert (CXP)** [18] includes 223,648 chest radiographs from a frontal or lateral view, which categorizes each image into 5 diseases: atelectasis, cardiomegaly, consolidation, edema, and pleural effusion. Aligned with [17, 61], we designate the expert-labeled official validation set as the test data. We randomly chose 5,000 radiographs from the training data as the validation set. The split for training/validation/testing comprises 218,414/5,000/234 images.

**RSNA Pneumonia** [43] is composed of 29,700 frontal-view chest radiographs, each accompanied by pneumonia opacity bounding boxes if pneumonia is present in the image. Four tasks are conducted on this dataset: fine-tune classification, linear classification, semantic segmentation, and object detection. For fine-tune and linear classification tasks, we adhere to the official data partitioning, allocating 25,184, 1,500, and 3,000 images for the training, validation, and test sets, respectively. In the context of semantic segmentation and object detection, our approach aligns with the methodology proposed in [49], wherein the original training set is randomly divided into subsets of 16,010, 5,337, and 5,337 samples for training, validation, and testing purposes, respectively.

**COVIDx CXR-3** [50] comprises 29,986 chest radiographs. This dataset presents a multi-class classification task, categorizing each image into *COVID-19*, *non-COVID pneumonia*, or *normal*. In line with [5, 48, 49], version 6 of this dataset is used. The official validation set is considered as our test data, and simultaneously, 10% of the original training set is randomly selected as validation data.

**SIIM-ACR Pneumothorax** [44] introduces the task of pneumothorax segmentation for evaluating the performance of segmentation models. This dataset includes 12,047 frontal-view chest radiographs with meticulously manually labeled pneumothorax masks. In accordance with [17], we partition the dataset into training/validation/test sets with a ratio of 70%/15%/15%.

### 4.3 Metrics

**AUC** and **ACC** are used for multi-label and multi-class classification, respectively. Specifically, we calculate the average AUC for each class. **Dice** is commonly measured for segmentation tasks, we set the threshold to 0.5 as default for all experiments. **mAP** is adopted for object detection. Following [49], we set the IOU thresholds to 0.4, 0.45, 0.5, 0.55, 0.6, 0.65, 0.7, 0.75, and report the average precision.

### 4.4 Implementation Details

We utilize an 8-layer ViT-B/16 [12] as the backbone for the image encoder and a 4-layer ViT-B/16 for the image decoder. Additionally, we employ BERT [11] as the text encoder. If not otherwise stated, we resize images to  $224 \times 224$  as input, except for super-resolution supervision we retain the  $448 \times 448$  resolution images. Texts are padded or truncated to a fixed length of 256 tokens. The latent dimension, denoted as  $D$ , is set to 768. The implementation is based on PyTorch [38]. For pre-training, our framework runs for 115 epochs on 4 NVIDIA A100 GPUs, taking approximately 20 hours. The training batch size is set to 256

**Table 3:** Comparison with other state-of-the-art methods fine-tuned on semantic segmentation and object detection task. † denotes performances reproduced using their officially released models. Methods with # leverage disease-level annotations, while Med-UniC [48] uses additional pre-training data. The best and second-best results are **bolded** and underlined.

Method	SIIM (Dice)			RSNA (Dice)			RSNA (mAP)		
	1%	10%	100%	1%	10%	100%	1%	10%	100%
Random init	9.0	28.6	54.3	6.9	10.6	18.5	1.0	4.0	8.9
ImageNet init	10.2	35.5	63.5	34.8	39.9	64.0	3.6	8.0	15.7
<i>CNN-based</i>									
MedKLIP# [54]	50.2	60.8	63.9	66.2	69.4	71.9	8.9	16.3	24.5
GLoRA [60]	35.8	46.9	63.4	59.3	67.5	67.8	9.8	14.8	18.8
SAT [31]	59.2	68.2	74.7	67.8	74.8	75.3	10.6	19.1	22.0
PRIOR [7]	54.6	63.7	76.8	68.7	71.9	74.4	13.8	20.5	25.6
MGCA# [49]	49.7	59.3	64.2	63.0	68.3	69.8	12.9	16.8	24.9
Med-Unic [48]	56.7	62.2	64.4	72.6	74.4	76.7	<u>16.6</u>	<u>22.3</u>	<b>31.1</b>
<i>ViT-based</i>									
†MGCA# [49]	62.7	65.2	71.4	75.2	<u>77.8</u>	<u>78.3</u>	8.9	19.2	26.3
†MRM [63]	<u>63.1</u>	<u>68.3</u>	78.4	74.2	77.6	78.2	11.5	20.3	27.1
Med-Unic [48]	62.1	67.3	71.5	<u>75.6</u>	76.6	77.9	-	-	-
MedIM [56]	-	63.5	81.3	-	-	-	-	-	-
ECAMP (Ours)	<b>67.3</b>	<b>70.4</b>	<b>84.5</b>	<b>77.1</b>	<b>78.6</b>	<b>79.5</b>	<b>19.8</b>	<b>25.8</b>	<u>31.0</u>

for each GPU, and we utilize a gradient accumulation step of 8. Consequently, the effective batch size reaches 8,192. We opt for AdamW [33] as our default optimizer, with a learning rate of 1.5e-4 and weight decay of 0.05. The values for  $\beta_1$  and  $\beta_2$  are set to 0.9 and 0.95, respectively. The mean squared error (MSE) loss is employed for masked image modeling and super-resolution, while cross-entropy loss is used for masked language modeling.

For the LLM in Eq. 1, we use GPT-3.5-turbo API [36] with setting temperature to 0 to distill 10,000 reports and fine-tune a Vicuna model [8] to distill the rest reports.

#### 4.5 Baselines

We conduct a comprehensive comparative analysis of ECAMP with numerous SOTA Med-VLP approaches *pre-trained solely on MIMIC-CXR* using ResNet-50 [16] (‘CNN-Based’) or ViT-B/16 [12] (‘ViT-Based’) as backbone, including MAE [15] trained on ImageNet [21] (denoted as ‘ImageNet init’), GLoRIA [17], REFERS [62], SAT [31], PRIOR [7], MedKLIP [54], MGCA [49], KAD [60], MedIM [56], and MRM [63]. Notably, Med-UniC [48] uses external multilingual datasets. In addition, we pre-train MAE [15] (denoted as ‘MAE’) and GLoRIA [17] with ViT-B/16 on MIMIC-CXR [19] using official source code. For MGCA, MRM, SAT, PRIOR, KAD, and MedKLIP whose official model are released, we fine-tune their models on the public downstream datasets in case there

**Table 4:** Ablation study of five simple-yet-effective components (*context distillation (CD)*, *descriptors masking (DM)*, *re-balanced factor (RF)*, *context-guided super-resolution (SR)*, and *MSCF*) proposed in ECAMP on multi-scale downstream tasks including fine-tune classification (CXR14 [51]), linear classification (COVIDx [50]), semantic segmentation (SIIM [44]), and object detection (RSNA [43]). All of the downstream tasks are trained with **1%** training data.

CD	DM	RF	SR	MSCF		CXR14 (AUC)	COVIDx (ACC)	SIIM (Dice)	RSNA (mAP)
				Global	Local				
×	×	×	×	✓	✓	79.5	78.0	65.4	4.1
✓	×	×	×	✓	✓	80.2	81.5	65.9	12.2
✓	✓	×	×	✓	✓	81.1	82.3	66.5	16.1
✓	✓	✓	×	✓	✓	81.5	83.0	66.6	14.9
×	✓	✓	✓	✓	✓	81.3	82.5	66.9	15.6
✓	×	✓	✓	✓	✓	81.4	83.0	66.4	16.8
✓	✓	×	✓	✓	✓	81.1	84.8	67.1	18.9
✓	✓	✓	✓	✓	×	81.8	85.0	65.7	12.6
✓	✓	✓	✓	×	✓	81.4	83.3	<b>67.5</b>	<b>20.4</b>
✓	✓	✓	✓	✓	✓	<b>81.9</b>	<b>86.3</b>	67.3	19.8

is no corresponding performance metrics in referenced papers. For MedIM and Med-UniC, whose official models are absent, we directly copy the performances from their papers for comparison.

## 5 Results

### 5.1 Results on Classification

We conduct both fine-tune and linear-probe with our ECAMP on four datasets, using 1%, 10%, and 100% of the training data, respectively. As in Table 1, our ECAMP significantly outperforms *all* CNN and ViT-based competitive Med-VLP models across different ratios of training data on the four datasets. It is worth noting that, on the ChestX-ray14 [51], *which encompasses the most of testing data and disease labels, ECAMP surpasses the strongest counterpart by 2.5% using only 1% labeled data*. For a comparison of 14 diseases, refer to Appendix.D. Surprisingly, on the COVIDx with a novel disease “COVID-19”, which is not present in MIMIC-CXR [19], a great performance gap can be found in Table 1 between ECAMP and SOTA methods. This validates the superiority of the representation learned by our ECAMP. Interestingly, we find the cross-modality

**Table 5:** Ablation study on parameter  $\lambda_{neg}$  proposed in Eq. 3 on fine-tuning (CXR14 [51]) and linear (COVIDx [50]) classification with different ratios of training data (1%, 10%).

$\lambda_{neg}$	CXR14 (AUC)		COVIDx (ACC)	
	1%	10%	1%	10%
0.025	81.7	84.5	85.0	93.3
<b>0.05</b>	<b>81.9</b>	<b>85.1</b>	<b>86.3</b>	<b>95.0</b>
0.1	81.8	84.6	80.5	94.8
0.25	81.5	84.2	79.5	94.0
0.5	81.4	84.2	82.5	91.5

reconstruction-based methods MRM [63] and our ECAMP outperform the contrastive-based methods like MGCA [49] and GloRIA [17]. Moreover, Table 2 presents the results of linear-probe classification. ECAMP exhibits consistently improved performance compared with SOTA methods on CXR14, RSNA and COVIDx datasets.

## 5.2 Results on Segmentation and Detection

To assess the effectiveness of local representations learned by ECAMP, extensive experiments on fine-grained downstream tasks including segmentation and detection are conducted in Table 3. Compared to strong SOTA approaches and boosted by MSCF, ECAMP makes remarkable improvements on all three datasets and ratios. Even in scenarios where MGCA [49] and MedKLIP [54] leverage disease-level labels, and Med-UniC [48] incorporates additional large-scale training data like PadChest [4], our ECAMP consistently outperforms all aforementioned methods. Distinguished Dice score leaps of 4.2% and 1.5% against SOTA methods are achieved on two segmentation datasets SIIM [44] and RSNA [43] using 1% training data, respectively. Notably, ECAMP reaches a Dice score of 67.3%, which outperforms CNN-based methods fine-tuned by 100% training data on SIIM [44]. Similarly, our method attains the best mAP using limited data on the object detection task. Remarkably, our method exhibits a significant lead of 8.3% compared to other SOTA open-source methods based on ViT. These achievements substantiate the effectiveness of ECAMP to optimize informative local features for fine-grained downstream tasks.

## 5.3 Ablation Study and Analysis

**Advantages of context distillation** The first row in Table 4 is trained by basic MIM and MLM. When we use the distilled easy-comprehensible report, we observe a performance improvement of 3.5% on COVIDx [50] and 0.7% on CXR14 [51]. Moreover, when we train ECAMP without the distilled report, notable performance degradation is observed, particularly on COVIDx and RSNA [43], validating the significant role of *entity-aware context distillation*.

**Effectiveness of descriptors masking** After constantly masking the critical descriptive words (as shown in Fig 2) preceding the entities, substantial performance enhancements are observed across both coarse-grained and fine-grained tasks, exceeding our initial expectations (as shown in Table 4). Accordingly, it is confirmed that *descriptors masking* can better leverage the supervised signals in medical reports.

**Sensitive analysis of the re-balanced factor** In the performance increment between the 3rd and the 4th rows as well as the 7th row and the last row of Table 4, we highlight the effectiveness of our proposed *re-balanced factor*. The AUC score increases by 0.9% and 0.8% respectively on CXR14, while the ACC shows sequential improvements of 0.7% and 1.5%. It is evident that the *re-balanced factor* primarily contributes to the performance of classification tasks. We further provide hyper-parameter analysis of  $\lambda_{neg}$  corresponding to different imbalance

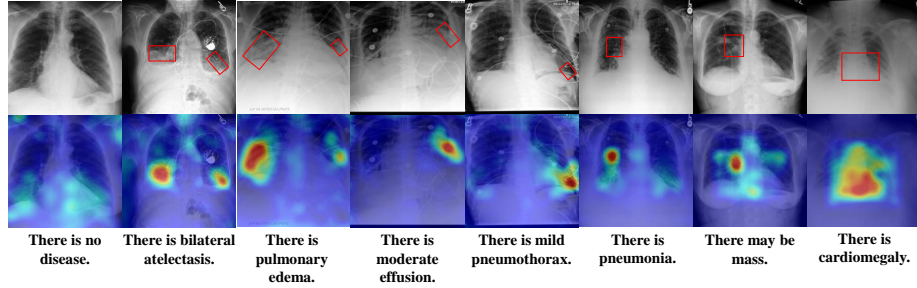


**Fig. 4:** Cross-attention maps between diagnosis and vision patterns learned by local aggregated features in MSCF, which successfully localizes the pathology region of various diseases.

ratios between positive and negative expressions. As shown in Table. 5, setting  $\lambda_{neg}$  to 0.05 according to the imbalance ratio (20:1) leads to best performance. **Performance of context-guided SR** As listed in the 4th row and the last row of Table 4, employing *context-guided SR* provides performance gains from 83.0% to 86.3% on COVIDx. Notably, on SIIM, the Dice score improves from 66.6% to 67.3% and mAP sees a notable increase of 4.9% on RSNA. This underscores the efficacy of *context-guided super resolution* in aiding pre-trained models to capture prior knowledge of visual texture structure, particularly enhancing performance in fine-grained visual downstream tasks.

**Contributions of MSCF** We exclusively integrate the global vision feature  $f_v^g$  and local aggregated feature  $f_a^l$  to predict the masked words respectively. The results in Table 4 validate that, only fusing  $f_v^g$  decreases the performances on low-level downstream tasks (segmentation and detection), while the classification performance relies on well-trained  $f_a^l$ . It is confirmed that *MSCF* successfully contributes to learning local and global representations and concurrently achieving SOTA performance on multi-scale downstream tasks.

**Representation analysis** As the attention map of the local vision feature and the corresponding distilled reports visualized in Fig. 4, the text modality of ECAMP captures the correct pathological regions of lung collapse (marked by red boxes) through cross-modal attention with the visual modality. Furthermore, there is no particularly disease-sensitive cross-attention for healthy images. These results support the ability of the *MSCF* to learn accurate and discriminative fine-grained representations, which is crucial for improving the performance of local downstream tasks.

## 6 Impact, Limitation, and Conclusion

In this paper, we confront the linguistic challenge of complex medical reports by distilling precise entity-centered knowledge using a large language model. Subsequently, the context-imbalanced issue is addressed by proposing a novel re-balanced factor, then entity-centered descriptors masking is proposed to strengthen

the entity-centered context for masked language modeling. Furthermore, a context-guided super-resolution learns to capture the critical pathology vision features with entity-awareness. In addition, multi-scale context fusion helps to optimize informative global and local representations simultaneously. These four readily accessible modules form the core of our simple-yet-effective framework, referred to as ECAMP, whose significant superior performance is validated on various public datasets on downstream tasks, including classification, segmentation, and classification. ECAMP facilitates the development of a robust medical foundation model, ultimately alleviating the workload of experts. However, the absence of explicit alignment between text and vision modalities hinders the application in zero-shot setting. In the future, we plan to incorporate contrastive learning to further empower ECAMP to function as an expert doctor without any manual annotation.

## References

1. Bannur, S., Hyland, S., Liu, Q., Perez-Garcia, F., Ilse, M., Castro, D.C., Boecking, B., Sharma, H., Bouzid, K., Thieme, A., et al.: Learning to exploit temporal structure for biomedical vision-language processing. In: CVPR. pp. 15016–15027 (2023) [2](#)
2. Boecking, B., Usuyama, N., Bannur, S., de Castro, D.C., Schwaighofer, A., Hyland, S.L., Wetscherek, M.T.A., Naumann, T., Nori, A., Alvarez-Valle, J., Poon, H., Oktay, O.: Making the most of text semantics to improve biomedical vision-language processing. In: ECCV (2022) [2](#), [5](#)
3. Brown, T., Mann, B., Ryder, N., Subbiah, M., Kaplan, J.D., Dhariwal, P., Neelakantan, A., Shyam, P., Sastry, G., Askell, A., et al.: Language models are few-shot learners. vol. 33, pp. 1877–1901 (2020) [3](#), [5](#)
4. Bustos, A., Pertusa, A., Salinas, J.M., de la Iglesia-Vayá, M.: Padchest: A large chest x-ray image dataset with multi-label annotated reports. *Medical image analysis* **66**, 101797 (2020) [13](#)
5. Chen, C., Zhong, A., Wu, D., Luo, J., Li, Q.: Contrastive masked image-text modeling for medical visual representation learning. pp. 493–503. Springer (2023) [5](#), [10](#)
6. Chen, Z., Du, Y., Hu, J., Liu, Y., Li, G., Wan, X., Chang, T.H.: Multi-modal masked autoencoders for medical vision-and-language pre-training. pp. 679–689. Springer (2022) [3](#), [5](#), [6](#)
7. Cheng, P., Lin, L., Lyu, J., Huang, Y., Luo, W., Tang, X.: Prior: Prototype representation joint learning from medical images and reports. In: ICCV. pp. 21361–21371 (2023) [3](#), [5](#), [8](#), [9](#), [11](#), [24](#), [25](#)
8. Chiang, W.L., Li, Z., Lin, Z., Sheng, Y., Wu, Z., Zhang, H., Zheng, L., Zhuang, S., Zhuang, Y., Gonzalez, J.E., Stoica, I., Xing, E.P.: Vicuna: An open-source chatbot impressing gpt-4 with 90%\* chatgpt quality (March 2023), <https://lmsys.org/blog/2023-03-30-vicuna/> [11](#), [21](#)
9. Cho, J., Lei, J., Tan, H., Bansal, M.: Unifying vision-and-language tasks via text generation. In: International Conference on Machine Learning. pp. 1931–1942. PMLR (2021) [4](#)
10. Dai, S., Wang, Q., Lyu, Y., Zhu, Y.: Bdkg at mediqa 2021: System report for the radiology report summarization task. In: Proceedings of the 20th Workshop on Biomedical Language Processing. pp. 103–111 (2021) [2](#), [3](#)
11. Devlin, J., Chang, M.W., Lee, K., Toutanova, K.: Bert: Pre-training of deep bidirectional transformers for language understanding (2018) [2](#), [5](#), [6](#), [7](#), [10](#)
12. Dosovitskiy, A., Beyer, L., Kolesnikov, A., Weissenborn, D., Zhai, X., Unterthiner, T., Dehghani, M., Minderer, M., Heigold, G., Gelly, S., et al.: An image is worth 16x16 words: Transformers for image recognition at scale. In: ICLR (2020) [6](#), [10](#), [11](#)
13. Erickson, B.J., Korfiatis, P., Akkus, Z., Kline, T.L.: Machine learning for medical imaging. *Radiographics* **37**(2), 505–515 (2017) [2](#)
14. Esteva, A., Kuprel, B., Novoa, R.A., Ko, J., Swetter, S.M., Blau, H.M., Thrun, S.: Dermatologist-level classification of skin cancer with deep neural networks. *nature* **542**(7639), 115–118 (2017) [2](#)
15. He, K., Chen, X., Xie, S., Li, Y., Doll’ar, P., Girshick, R.B.: Masked autoencoders are scalable vision learners. In: CVPR. pp. 15979–15988 (2021) [2](#), [5](#), [6](#), [8](#), [9](#), [11](#), [25](#)
16. He, K., Zhang, X., Ren, S., Sun, J.: Deep residual learning for image recognition. In: Proceedings of the IEEE conference on computer vision and pattern recognition. pp. 770–778 (2016) [11](#)

17. Huang, S.C., Shen, L., Lungren, M.P., Yeung, S.: Gloria: A multimodal global-local representation learning framework for label-efficient medical image recognition. In: ICCV. pp. 3942–3951 (2021) [2](#), [3](#), [4](#), [7](#), [8](#), [9](#), [10](#), [11](#), [13](#), [24](#), [25](#)
18. Irvin, J., Rajpurkar, P., Ko, M., Yu, Y., Ciurea-Ilcus, S., Chute, C., Marklund, H., Haghighi, B., Ball, R., Shpanskaya, K., et al.: Chexpert: A large chest radiograph dataset with uncertainty labels and expert comparison. In: Proceedings of the AAAI conference on artificial intelligence. vol. 33, pp. 590–597 (2019) [3](#), [10](#)
19. Johnson, A.E., Pollard, T.J., Berkowitz, S.J., Greenbaum, N.R., Lungren, M.P., Deng, C.y., Mark, R.G., Horng, S.: MIMIC-CXR, a de-identified publicly available database of chest radiographs with free-text reports. *Scientific data* **6**(1), 1–8 (2019) [3](#), [9](#), [11](#), [12](#)
20. Johnson, A.E., Pollard, T.J., Greenbaum, N.R., Lungren, M.P., Deng, C.y., Peng, Y., Lu, Z., Mark, R.G., Berkowitz, S.J., Horng, S.: MIMIC-CXR-JPG, a large publicly available database of labeled chest radiographs. arXiv preprint arXiv:1901.07042 (2019) [9](#)
21. Krizhevsky, A., Sutskever, I., Hinton, G.E.: Imagenet classification with deep convolutional neural networks. *Communications of the ACM* **60**(6), 84–90 (2017) [11](#)
22. Li, C.Y., Liang, X., Hu, Z., Xing, E.P.: Knowledge-driven encode, retrieve, paraphrase for medical image report generation. In: AAAI. vol. 33, pp. 6666–6673 (2019) [2](#)
23. Li, J., Li, D., Xiong, C., Hoi, S.: Blip: Bootstrapping language-image pre-training for unified vision-language understanding and generation. In: International Conference on Machine Learning. pp. 12888–12900. PMLR (2022) [4](#)
24. Li, J., Selvaraju, R., Gotmare, A., Joty, S., Xiong, C., Hoi, S.C.H.: Align before fuse: Vision and language representation learning with momentum distillation. *Advances in neural information processing systems* **34**, 9694–9705 (2021) [4](#)
25. Li, L.H., Zhang, P., Zhang, H., Yang, J., Li, C., Zhong, Y., Wang, L., Yuan, L., Zhang, L., Hwang, J.N., et al.: Grounded language-image pre-training. In: Proceedings of the IEEE/CVF Conference on Computer Vision and Pattern Recognition. pp. 10965–10975 (2022) [4](#)
26. Li, W., Gao, C., Niu, G., Xiao, X., Liu, H., Liu, J., Wu, H., Wang, H.: Unimodal: Towards unified-modal understanding and generation via cross-modal contrastive learning. arXiv preprint arXiv:2012.15409 (2020) [4](#)
27. Li, X., Yin, X., Li, C., Zhang, P., Hu, X., Zhang, L., Wang, L., Hu, H., Dong, L., Wei, F., et al.: Oscar: Object-semantic aligned pre-training for vision-language tasks. In: ECCV. pp. 121–137 (2020) [4](#)
28. Li, Y., Fan, H., Hu, R., Feichtenhofer, C., He, K.: Scaling language-image pre-training via masking. arXiv preprint arXiv:2212.00794 (2022) [4](#)
29. Li, Y., Liang, X., Hu, Z., Xing, E.P.: Hybrid retrieval-generation reinforced agent for medical image report generation. In: NeurIPS. vol. 31 (2018) [2](#)
30. Lipscomb, C.E.: Medical subject headings (mesh). *Bulletin of the Medical Library Association* **88**(3), 265 (2000) [3](#), [5](#), [21](#)
31. Liu, B., Lu, D., Wei, D., Wu, X., Wang, Y., Zhang, Y., Zheng, Y.: Improving medical vision-language contrastive pretraining with semantics-aware triage. *IEEE Transactions on Medical Imaging* (2023) [4](#), [8](#), [9](#), [11](#), [24](#)
32. Liu, F., Zhu, T., Wu, X., Yang, B., You, C., Wang, C., Lu, L., Liu, Z., Zheng, Y., Sun, X., et al.: A medical multimodal large language model for future pandemics. *NPJ Digital Medicine* **6**(1), 226 (2023) [5](#)
33. Loshchilov, I., Hutter, F.: Decoupled weight decay regularization. arXiv preprint arXiv:1711.05101 (2017) [11](#)

34. Min, S., Lyu, X., Holtzman, A., Artetxe, M., Lewis, M., Hajishirzi, H., Zettlemoyer, L.: Rethinking the role of demonstrations: What makes in-context learning work? pp. 11048–11064 (2022) [6](#)
35. Mu, N., Kirillov, A., Wagner, D., Xie, S.: Slip: Self-supervision meets language-image pre-training. In: European Conference on Computer Vision. pp. 529–544. Springer (2022) [4](#)
36. OpenAI: Gpt-4 technical report. arXiv preprint arXiv:2303.08774 (2023) [3](#), [11](#), [21](#), [22](#)
37. Ouyang, L., Wu, J., Jiang, X., Almeida, D., Wainwright, C., Mishkin, P., Zhang, C., Agarwal, S., Slama, K., Ray, A., et al.: Training language models to follow instructions with human feedback. vol. 35, pp. 27730–27744 (2022) [5](#)
38. Paszke, A., Gross, S., Massa, F., Lerer, A., Bradbury, J., Chanan, G., Killeen, T., Lin, Z., Gimelshein, N., Antiga, L., et al.: Pytorch: An imperative style, high-performance deep learning library. *Advances in neural information processing systems* **32** (2019) [10](#)
39. Pathak, Y., Shukla, P.K., Tiwari, A., Stalin, S., Singh, S.: Deep transfer learning based classification model for covid-19 disease. *Irbm* **43**(2), 87–92 (2022) [2](#)
40. Pellegrini, C., Keicher, M., Özsoy, E., Jiraskova, P., Braren, R., Navab, N.: Xplainer: From x-ray observations to explainable zero-shot diagnosis (2023) [2](#)
41. Radford, A., Kim, J.W., Hallacy, C., Ramesh, A., Goh, G., Agarwal, S., Sastry, G., Askell, A., Mishkin, P., Clark, J., et al.: Learning transferable visual models from natural language supervision. In: International Conference on Machine Learning. pp. 8748–8763. PMLR (2021) [4](#)
42. Sanh, V., Webson, A., Raffel, C., Bach, S.H., Sutawika, L., Alyafeai, Z., Chaffin, A., Stiegler, A., Le Scao, T., Raja, A., et al.: Multitask prompted training enables zero-shot task generalization. In: ICLR (2022) [5](#)
43. Shih, G., Wu, C.C., Halabi, S.S., Kohli, M.D., Prevedello, L.M., Cook, T.S., Sharma, A., Amorosa, J.K., Arteaga, V., Galperin-Aizenberg, M., et al.: Augmenting the national institutes of health chest radiograph dataset with expert annotations of possible pneumonia. *Radiology: Artificial Intelligence* **1**(1), e180041 (2019) [3](#), [10](#), [12](#), [13](#)
44. Steven G. Langer, PhD, C., George Shih, MD, M.: Siim-acr pneumothorax segmentation (2019) [3](#), [10](#), [12](#), [13](#)
45. Su, C.Y., Mcmillan, C.: Distilled gpt for source code summarization (2023) [5](#)
46. Titano, J.J., Badgeley, M., Schefflein, J., Pain, M., Su, A., Cai, M., Swinburne, N., Zech, J., Kim, J., Bederson, J., et al.: Automated deep-neural-network surveillance of cranial images for acute neurologic events. *Nature medicine* **24**(9), 1337–1341 (2018) [2](#)
47. Tiu, E., Talius, E., Patel, P., Langlotz, C.P., Ng, A.Y., Rajpurkar, P.: Expert-level detection of pathologies from unannotated chest x-ray images via self-supervised learning. *Nature Biomedical Engineering* **6**(12), 1399–1406 (2022) [4](#)
48. Wan, Z., Liu, C., Zhang, M., Fu, J., Wang, B., Cheng, S., Ma, L., Quilodrán-Casas, C., Arcucci, R.: Med-unic: Unifying cross-lingual medical vision-language pre-training by diminishing bias. In: NeurIPS (2023) [5](#), [9](#), [10](#), [11](#), [13](#)
49. Wang, F., Zhou, Y., Wang, S., Vardhanabhuti, V., Yu, L.: Multi-granularity cross-modal alignment for generalized medical visual representation learning (2022) [2](#), [4](#), [5](#), [8](#), [9](#), [10](#), [11](#), [13](#), [25](#)
50. Wang, L., Lin, Z.Q., Wong, A.: Covid-net: A tailored deep convolutional neural network design for detection of covid-19 cases from chest x-ray images. *Scientific reports* **10**(1), 1–12 (2020) [3](#), [10](#), [12](#), [13](#)

51. Wang, X., Peng, Y., Lu, L., Lu, Z., Bagheri, M., Summers, R.M.: Chestx-ray8: Hospital-scale chest x-ray database and benchmarks on weakly-supervised classification and localization of common thorax diseases. In: Proceedings of the IEEE conference on computer vision and pattern recognition. pp. 2097–2106 (2017) [3](#), [9](#), [12](#), [13](#)
52. Wang, Z., Yu, J., Yu, A.W., Dai, Z., Tsvetkov, Y., Cao, Y.: Simvlm: Simple visual language model pretraining with weak supervision. In: International Conference on Learning Representations [4](#)
53. Wei, J., Bosma, M., Zhao, V., Guu, K., Yu, A.W., Lester, B., Du, N., Dai, A.M., Le, Q.V.: Finetuned language models are zero-shot learners. In: ICLR (2021) [6](#)
54. Wu, C., Zhang, X., Zhang, Y., Wang, Y., Xie, W.: Medklip: Medical knowledge enhanced language-image pre-training. In: ICCV (2023) [5](#), [8](#), [9](#), [11](#), [13](#)
55. Wu, Y., Schuster, M., Chen, Z., Le, Q.V., Norouzi, M., Macherey, W., Krikun, M., Cao, Y., Gao, Q., Macherey, K., et al.: Google’s neural machine translation system: Bridging the gap between human and machine translation. arXiv preprint arXiv:1609.08144 (2016) [6](#)
56. Xie, Y., Gu, L., Harada, T., Zhang, J., Xia, Y., Wu, Q.: Medim: Boost medical image representation via radiology report-guided masking. pp. 13–23. Springer (2023) [5](#), [9](#), [11](#)
57. Zhang, K., Yang, Y., Yu, J., Jiang, H., Fan, J., Huang, Q., Han, W.: Multi-task paired masking with alignment modeling for medical vision-language pre-training. IEEE Transactions on Multimedia (2023) [5](#)
58. Zhang, P., Li, X., Hu, X., Yang, J., Zhang, L., Wang, L., Choi, Y., Gao, J.: Vinvl: Revisiting visual representations in vision-language models. In: CVPR. pp. 5579–5588 (2021) [4](#)
59. Zhang, T., Ladhak, F., Durmus, E., Liang, P., McKeown, K., Hashimoto, T.B.: Benchmarking large language models for news summarization. arXiv preprint arXiv:2301.13848 (2023) [5](#)
60. Zhang, X., Wu, C., Zhang, Y., Xie, W., Wang, Y.: Knowledge-enhanced visual-language pre-training on chest radiology images. Nature Communications **14**(1), 4542 (2023) [5](#), [8](#), [9](#), [11](#), [24](#), [25](#)
61. Zhang, Y., Jiang, H., Miura, Y., Manning, C.D., Langlotz, C.P.: Contrastive learning of medical visual representations from paired images and text. arXiv preprint arXiv:2010.00747 (2020) [2](#), [4](#), [10](#)
62. Zhou, H.Y., Chen, X., Zhang, Y., Luo, R., Wang, L., Yu, Y.: Generalized radiograph representation learning via cross-supervision between images and free-text radiology reports. Nature Machine Intelligence **4**(1), 32–40 (2022) [4](#), [8](#), [11](#), [24](#)
63. Zhou, H.Y., Lian, C., Wang, L., Yu, Y.: Advancing radiograph representation learning with masked record modeling. In: ICLR (2023) [2](#), [3](#), [5](#), [6](#), [8](#), [9](#), [11](#), [13](#), [24](#), [25](#)
64. Zhou, S.K., Greenspan, H., Davatzikos, C., Duncan, J.S., Van Ginneken, B., Madabhushi, A., Prince, J.L., Rueckert, D., Summers, R.M.: A review of deep learning in medical imaging: Imaging traits, technology trends, case studies with progress highlights, and future promises. Proceedings of the IEEE (2021) [2](#)

## Appendix

### A Statistics of descriptive words

As illustrated in Fig. S1, we present the statistics of our defined descriptive words across 227,835 reports. Specifically, we focus on descriptors with a frequency greater than 10,000 among the total of 31,597 terms. Notably, only "may be" and "there is" imply uncertainty about the existence of the entity, such as a disease or radiology finding. The term "concerning for" can be used to indicate a doctor's assessment of the presence of a disease based on the interpretation of imaging results. It can also be preceded by "no" to convey the certainty of the absence of a particular disease. With the exception of the descriptive words mentioned above, all other terms listed in Fig. S1 indicate the semantic notion that the entity is absent. Appropriately, the quantity of negative descriptive words is  $20\times$  greater than that of the positive ones. Thus we propose a rebalanced factor to reweight the loss function to compensate for the dataset bias. Table 5 in the manuscript demonstrates that our re-balanced factor designed according to statistics contributes significantly to the improvements on multiple downstream tasks.

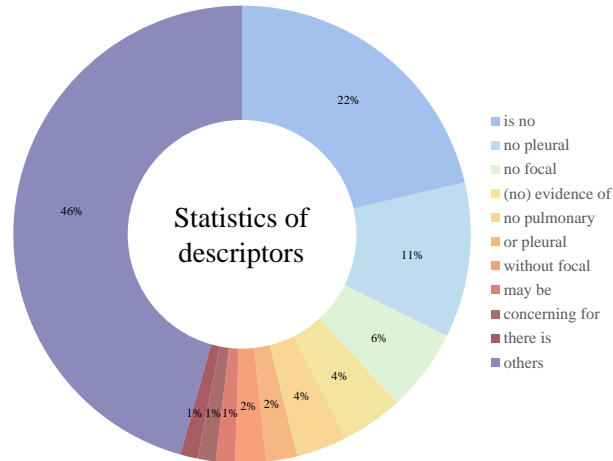


**Fig. S1:** The statistics of descriptive words, here we only show the statistics of descriptors with a frequency greater than 10,000, otherwise, the terms are collectively included in the category labeled as "others".

**Table S1:** Our selected entities. We select 44 entities based on their importance and frequency of appearance in radiology reports as comprehensively as possible.

Entities			
abnormality	abscess	aerate	aorta
atelectasis	bronchiectasis	calcification	cardiomediastinal
cardiomegaly	catheter	chf	collapse
congestion	consolidation	contour	COPD
deformity	dilation	distention	edema
effusion	embolism	emphysema	engorgement
fibrosis	fracture	granuloma	hernia
hilar	hyperinflate	hemidiaphragm	infiltrate
mass	nodule	obscure	opacity
perihilar	pneumonia	pneumothorax	sarcoidosis
silhouette	thickening	tuberculosis	vasculature

## B Selected entities

As shown in Table S1, we manually curate a list of 44 entities, including diseases or symptoms, sourced from Medical Subject Headings (MESH [30]). The selection is guided by their importance and the frequency of appearance in radiology reports. Future work involves including more entities, particularly some rare diseases.

## C Prompt used to distill reports, and examples of distilled reports

Table S2 displays the prompt utilized for report distillation. By inputting the radiology report as the content to ChatGPT [36] with this specific prompt, we obtain a distilled report that includes more detailed semantics regarding the existence and severity of entities. Specifically, using GPT3.5-turbo API [36] setting temperature with 0 to generate 10,000 distilled reports, we train a Vicuna7B [8] to further distill all the reports. Examples of these distilled reports are presented in Table S3.

**Table S2:** Our prompt used for report distillation is designed to include both an indication and an example. Providing ChatGPT [36] with an example of the task helps enhance its performance in generating distilled reports.

```

Messages = [
  { "role": "user", "content": f""" You are a knowledgeable radiologist. please help me analysis the medical reports and write brief and clear conclusions. Now, I will give you a medical report, as well as the mentioned entities. Please make conclusions according the medical reports, and write brief and clear conclusions as the following format: 'There is [a] [b].' when you are sure whether the entity exists in the report, or 'There may [a] [b].', when you are not sure whether the entity exists in the report. [a] represents adjective words describing the severeness of the entity [b]. Please generate conclusions for the entities mentioned above one by one, according to the format and do not generate other words. Please keep only one entity in a sentence, there is no need of using 'and' or 'or' to connect two or more words.
  """ },
  { "role": "user", "content": f"""
  —Example—
  Report: as compared to the lung volumes have slightly decreased. signs of mild over inflation and moderate pleural effusion persist. elongation of the descending aorta.
  Entities: aorta, inflation, effusion
  Conclusion:
  There is moderate pleural effusion.
  There is mild over inflation.
  There is descending aorta.
  —Example END—
  Given the report: {report}
  Entities: {entity}.
  Conclusion:
  """}]

```

## D Detailed performances on ChestX-ray14

As illustrated in Table S4 and Table S5, we provide a detailed presentation of the results, evaluating the classification performance in both fine-tuning and linear settings. In the fine-tuning setting, our method achieves state-of-the-art results, particularly in atelectasis, consolidation, mass, and pneumonia. However, the performance on edema, emphysema and fibrosis is notably lower. In the linear

**Table S3:** Examples of report distillation are presented. For each report, we showcase how the semantics of our selected entities are distilled by a large language model. The distilled reports provide more specificity regarding the existence of entities.

<b>Original Report</b>	There is no focal consolidation, pleural effusion, vascular congestion or pneumothorax. The cardiac hilar and mediastinal contours within normal limits.
<b>Distilled Report</b>	There is no consolidation. There is no pleural effusion. There is no vascular congestion. There is no pneumothorax. There is normal cardiac hilar. There are mediastinal contours.
<b>Original Report</b>	The lungs are clear of airspace or interstitial opacity. The cardiomediastinal silhouette is unremarkable. No pleural effusion or pneumothorax. No acute or aggressive osseous changes. No evidence of active or latent tb.
<b>Distilled Report</b>	There is no opacity. There is unremarkable cardiomediastinal silhouette. There is no pleural effusion. There is no pneumothorax.
<b>Original Report</b>	Right lower lobe opacity with an associated effusion could represent atelectasis or pneumonia.
<b>Distilled Report</b>	There is opacity. There may be atelectasis or pneumonia in the right lower lobe. There is an associated effusion.

setting, our method continues to achieve cutting-edge results, especially in consolidation, effusion, and pneumothorax. Similarly, our method faces challenges in edema classification. Future work will prioritize enhancing the classification performance for diseases with suboptimal accuracy.

**Table S4:** Detailed performance when fine-tuning the model for classification on ChestX-ray14. † denotes our reproduced results using their officially released models. The best and second-best results are **bolded** and underlined.

Data Ratio	Method	Average	Atelectasis	Cardiomegaly	Consolidation	Edema	Effusion	Emphysema	Fibrosis	Hernia	Infiltration	Mass	Nodule	Pleural Thickening	Pneumonia	Pneumothorax
1%	<i>CNN-based</i>															
	†GLORIA [17]	70.7	69.9	69.7	<u>82.9</u>	65.0	66.7	62.8	65.7	80.0	<u>74.4</u>	81.5	75.0	63.5	66.9	66.1
	†SAT [31]	67.4	71.9	70.7	<u>82.5</u>	68.5	63.3	59.4	61.2	75.7	72.4	83.4	65.3	55.3	64.3	50.6
	†PRIOR [7]	75.7	75.8	74.0	<b>85.8</b>	67.4	72.5	68.4	71.3	83.1	<b>80.5</b>	<b>86.5</b>	<u>76.9</u>	69.5	<b>71.3</b>	75.8
	KAD [60]	78.7	77.0	<u>88.2</u>	<u>82.9</u>	69.2	75.1	69.7	<u>73.5</u>	86.1	72.7	81.3	<b>89.3</b>	<b>74.3</b>	69.2	<b>93.8</b>
	<i>ViT-based</i>															
	REFERS [62]	76.7	77.5	85.6	78.6	84.9	85.4	79.5	72.3	77.1	67.5	76.2	66.5	71.6	69.3	81.7
	MRM [63]	<u>79.4</u>	<u>78.8</u>	<b>90.3</b>	80.0	<u>86.5</u>	<u>86.9</u>	<u>82.0</u>	71.9	<u>90.0</u>	67.2	82.3	69.6	72.3	69.6	84.0
	ECAMP (Ours)	<b>81.9</b>	<b>80.4</b>	<b>90.3</b>	80.5	<b>88.2</b>	<b>87.4</b>	<b>88.8</b>	<b>77.0</b>	<b>94.1</b>	68.6	<u>85.0</u>	74.0	<u>73.4</u>	<u>70.6</u>	<u>87.8</u>
	10%	<i>CNN-based</i>														
†GLORIA [17]		78.6	77.0	83.6	<u>84.9</u>	66.7	77.8	70.6	71.3	83.8	77.7	85.2	<u>88.7</u>	76.6	73.8	84.3
†SAT [31]		79.3	80.9	83.9	<b>87.3</b>	69.7	81.4	73.1	74.3	86.0	<b>80.1</b>	<u>87.7</u>	86.9	76.5	74.2	67.5
†PRIOR [7]		79.4	78.1	82.2	86.4	68.7	78.4	72.9	72.3	84.5	<u>79.2</u>	87.3	87.9	77.6	74.2	81.4
KAD [60]		80.7	77.6	88.9	83.3	71.8	78.3	71.9	73.7	87.2	75.0	83.3	<b>90.3</b>	<b>80.7</b>	72.3	<b>95.3</b>
<i>ViT-based</i>																
REFERS [62]		80.9	80.1	<u>89.8</u>	79.5	87.8	87.5	88.2	77.2	86.1	69.6	82.0	72.8	74.2	72.2	85.6
MRM [63]		<u>84.0</u>	<u>82.3</u>	<b>90.9</b>	81.1	<u>89.0</u>	<u>88.8</u>	<u>92.2</u>	<u>84.8</u>	<u>94.0</u>	70.1	86.6	75.1	78.6	<u>74.3</u>	88.4
ECAMP (Ours)		<b>85.1</b>	<b>83.9</b>	<b>90.9</b>	81.3	<b>89.8</b>	<b>89.1</b>	<b>92.6</b>	<b>86.3</b>	<b>95.6</b>	71.3	<b>87.8</b>	79.0	<u>79.0</u>	<b>76.0</b>	<u>89.3</u>
100%		<i>CNN-based</i>														
	†GLORIA [17]	84.1	82.5	89.1	<u>88.5</u>	71.3	85.0	77.6	76.3	88.5	<u>81.3</u>	<u>90.0</u>	<u>92.8</u>	<b>83.1</b>	<u>78.4</u>	92.7
	†SAT [31]	83.7	82.0	90.0	87.8	69.6	83.9	77.5	75.5	88.8	79.9	89.6	92.4	82.7	78.2	<u>93.9</u>
	†PRIOR [7]	84.3	82.7	89.4	<b>88.9</b>	71.7	85.2	77.9	76.6	88.9	<b>81.7</b>	<b>90.5</b>	<b>93.3</b>	82.6	77.9	93.3
	KAD [60]	82.5	78.5	89.7	84.0	71.3	83.6	77.1	74.0	87.4	75.3	86.0	91.6	<u>82.9</u>	77.8	<b>96.1</b>
	<i>ViT-based</i>															
	REFERS [62]	84.7	83.0	92.3	82.1	90.2	88.7	91.4	83.9	93.3	74.1	85.5	76.7	78.5	77.0	89.1
	MRM [63]	<u>85.9</u>	<u>84.2</u>	<u>93.0</u>	82.2	<u>91.0</u>	<u>89.6</u>	<u>94.3</u>	<u>86.7</u>	<u>94.4</u>	71.8	88.2	78.5	81.4	77.3	90.2
	ECAMP (Ours)	<b>86.7</b>	<b>85.1</b>	<b>93.1</b>	82.3	<b>91.1</b>	<b>89.7</b>	<b>94.5</b>	<b>87.9</b>	<b>96.0</b>	72.7	88.9	81.4	81.7	<b>78.5</b>	91.0

**Table S5:** Detailed performance of linear classification on ChestX-ray14. † denotes our reproduced results using their officially released models or our reproduction on MIMIC-CXR. Methods with # leverage disease-level annotations. The best and second-best results are **bolded** and underlined.

Data Ratio	Method	Average	Atelectasis	Cardiomegaly	Consolidation	Edema	Effusion	Emphysema	Fibrosis	Hernia	Infiltration	Mass	Nodule	Pleural Thickening	Pneumonia	Pneumothorax	
1%	<i>CNN-based</i>																
	†PRIOR [7]	74.9	73.2	84.7	78.2	69.2	78.0	65.2	64.8	81.7	70.2	80.9	78.6	70.1	65.4	84.4	
	†KAD [60]	78.1	77.9	85.1	<u>87.4</u>	68.6	78.3	69.0	69.7	86.3	77.1	<b>88.4</b>	<u>84.7</u>	72.8	69.6	78.0	
	<i>ViT-based</i>																
	†MAE [15]	75.1	72.4	81.8	79.6	69.6	76.6	64.3	65.8	80.5	76.1	80.6	80.2	72.3	<u>71.3</u>	80.2	
	†GLORIA [17]	77.0	75.5	82.9	82.2	66.5	75.9	67.6	67.7	82.1	78.1	84.1	84.3	<u>79.9</u>	72.9	84.4	
	†MGCA# [49]	78.7	77.0	<u>88.3</u>	86.3	68.1	<u>78.6</u>	68.8	69.4	85.1	<u>78.3</u>	87.5	<b>85.1</b>	<b>74.2</b>	69.5	<u>85.2</u>	
	†MRM [63]	<u>78.8</u>	<u>79.6</u>	82.9	<b>88.1</b>	<u>69.9</u>	75.9	<u>69.1</u>	<u>70.4</u>	<u>87.2</u>	<b>81.6</b>	<b>89.8</b>	83.9	71.5	<b>71.7</b>	82.2	
	ECAMP (Ours)	<b>81.0</b>	<b>80.2</b>	<b>88.4</b>	80.8	<b>88.1</b>	<b>87.8</b>	<b>87.1</b>	<b>76.0</b>	<b>92.2</b>	68.1	82.6	71.4	73.0	<u>71.3</u>	<b>87.6</b>	
	10%	<i>CNN-based</i>															
		†PRIOR [7]	79.5	80.2	85.1	87.4	69.7	79.0	72.8	74.3	80.6	80.0	77.9	79.5	80.9	75.8	89.5
†KAD [60]		79.8	79.2	84.2	<u>88.1</u>	69.5	77.9	72.7	67.3	85.5	77.4	<u>90.1</u>	89.4	74.5	71.3	90.3	
<i>ViT-based</i>																	
†MAE [15]		79.7	80.3	87.1	81.8	70.5	77.8	71.6	72.3	86.0	79.5	85.2	81.5	78.0	75.8	88.7	
†GLORIA [17]		81.9	80.6	88.3	87.5	69.8	81.8	72.7	73.0	86.5	79.7	87.3	90.0	<u>82.6</u>	76.5	89.4	
†MGCA# [49]		82.7	81.5	<u>90.4</u>	87.9	70.6	<u>82.4</u>	<u>72.8</u>	<u>74.7</u>	87.0	<u>80.2</u>	89.2	<u>90.8</u>	<b>82.9</b>	<u>76.7</u>	<u>90.5</u>	
†MRM [63]		<u>82.7</u>	<u>82.3</u>	85.9	<b>88.5</b>	<u>71.7</u>	81.6	72.2	74.2	<u>88.0</u>	<b>81.1</b>	<b>90.7</b>	<b>91.0</b>	81.7	<b>77.3</b>	<b>90.8</b>	
ECAMP (Ours)		<b>83.8</b>	<b>82.5</b>	<b>90.6</b>	81.2	<b>89.7</b>	<b>88.9</b>	<b>90.9</b>	<b>84.4</b>	<b>91.2</b>	70.8	85.1	75.6	78.4	75.4	88.8	
100%		<i>CNN-based</i>															
		†PRIOR [7]	82.1	82.7	90.8	88.7	71.2	83.0	73.1	76.2	88.5	81.4	89.2	85.9	81.8	74.7	82.3
	†KAD [60]	81.6	81.6	90.8	88.4	70.3	82.6	72.1	73.4	84.0	80.8	89.3	90.8	80.8	72.9	83.8	
	<i>ViT-based</i>																
	†MAE [15]	82.9	82.3	91.1	87.8	70.5	82.8	73.6	75.3	86.0	80.5	88.2	89.5	84.1	77.8	90.7	
	†GLORIA [17]	83.8	82.0	<u>91.7</u>	88.5	70.0	84.0	74.5	77.3	88.2	80.4	89.8	91.6	<b>85.0</b>	78.1	92.1	
	†MGCA# [49]	84.1	82.6	<b>91.9</b>	88.6	71.3	83.4	75.1	77.2	88.6	81.1	90.0	<b>92.0</b>	<u>84.4</u>	<u>78.2</u>	<u>92.8</u>	
	†MRM [63]	<u>84.6</u>	<u>83.4</u>	<u>91.7</u>	<b>88.8</b>	<u>71.8</u>	<u>86.1</u>	<u>76.7</u>	<u>77.5</u>	<u>89.8</u>	81.6	<b>90.2</b>	<u>91.8</u>	83.9	<b>78.4</b>	<b>92.9</b>	
	ECAMP (Ours)	<b>85.1</b>	<b>83.5</b>	91.5	81.6	<b>90.5</b>	<b>89.2</b>	<b>92.2</b>	<b>86.2</b>	<b>95.6</b>	71.2	85.7	76.6	80.2	77.7	90.1	